A General Strategy to Glassy M-Te (M=Ru, Rh, Ir) Porous Nanorods as Efficient Electrocatalysts for N_2 Reduction

Juan Wang, Bolong Huang, Mingzi Sun, Tong Wu, Yujin Ji, Rongguan Yin, Xing Zhu, Youyong Li, Qi Shao, and Xiaoqing Huang**

J. Wang, R. Yin, Dr. Q. Shao, Prof. X. Huang

College of Chemistry, Chemical Engineering and Materials Science, Soochow University, Jiangsu, 215123, P. R. China

Email: hxq006@suda.edu.cn

Prof. B. Huang, M. Sun, T. Wu

Department of Applied Biology and Chemical Technology, The Hong Kong Polytechnic University, Hung Hom, Kowloon, Hong Kong SAR, China

Email: bhuang@polyu.edu.hk

Y. Ji, Prof. Y. Li

Institute of Functional Nano & Soft Materials (FUNSOM), Soochow University, Jiangsu, 215123, P. R. China

Dr. X. Zhu

Testing & Analysis Center, Soochow University, Jiangsu, 215123, P. R. China

Abstract: Electrochemically converting nitrogen (N_2) into value-added ammonia (NH_3) is highly desirable yet formidably challenging due to the extreme inertness of the N_2 molecule, which makes developing a robust electrocatalyst prerequisite. Herein, we report a new class of bullet-like MTe (M=Ru, Rh, Ir) glassy porous nanorods (PNRs) as excellent electrocatalysts for N_2 reduction reaction (NRR). The optimized $IrTe_4$ PNRs present superior activity with the highest NH_3 yield (51.1 μg h^{-1} $mg^{-1}_{cat.}$) and Faraday efficiency (15.3%) as well as long-term stability of up to 20 consecutive cycles, making them among the most active NRR electrocatalysts reported to date. Both the N_2 temperature-programmed desorption and valence band X-ray photoelectron spectroscopy data show that the strong chemical adsorption

of nitrogen species is the key for enhancing NRR and suppressing the hydrogen evolution reaction (HER) of $IrTe_4$ PNRs. DFT calculations comprehensively identify the superior adsorption strength of $IrTe_4$ adsorptions originates from the synergistic collaboration between electron-rich Ir and the highly electroactive surrounding Te atoms. The optimal adsorption of both N_2 and H_2O in alkaline media guarantee the superior consecutive NRR process. This work opens a new avenue for designing high-performance NRR electrocatalysts based on glassy materials.

Keywords: Glassy • Ir • Te • N_2 reduction reaction • nanorod

Introduction

Ammonia (NH_3), as a critical energy carrier, plays a key role in various fields such as agriculture, medicine and chemical industries.[1] The fixation of atmospheric nitrogen (N_2) to generate NH_3 was mainly achieved by biological pathway before the 1900s, where the features of being susceptible to inactivity and inefficiency of nitrogenase largely hindered their practical application.[2] Subsequently, the Haber-Bosch process has been employed as a large scalable method to produce NH_3 in industry; however, high energy consumption (300-500 °C and 150-300 atm) and large carbon dioxide emission (CO_2) (1.5 tons of CO_2 per ton of NH_3 made) pose severe challenges to environmental pollution and ecological degradation.[3] As a milder, greener and more efficient strategy, electrochemical N_2 reduction reaction (NRR) offers a more attractive way to N_2 conversion.[4] However, the dissociation of highly inert N_2 molecule renders the NRR difficult under atmospheric conditions due to the strong bond energy of the N≡N triple bond (940.95 kJ mol-1).[5] Moreover, the hydrogen evolution reaction (HER), which has faster reaction kinetics under similar potential, is the major competitive reaction during the NRR process.[6] Therefore, developing efficient catalysts with

robust activation ability to break the N≡N triple bond for N_2 conversion while suppressing HER is extremely desirable.

To overcome the above issues, several metallic elements with optimized nitrogen binding ability have been reported as NRR electrocatalysts in experimental and theoretical studies.[7] However, the tendency of their surface to be easily covered by adsorbed H causes the active site to drastically decrease for NRR.[8] Ultimately, the strategy of combining with non-metals may be a practical way to weaken the binding of adsorbed H for suppressing HER. Qiao et al. used layered W_2N_3 nanosheet with nitrogen vacancies as an active NRR electrocatalyst under alkaline conditions, where the Faradic efficiency (FE) and NH_3 yield achieved were 11.6 μg h^{-1} $mg^{-1}_{cat.}$ and 11.67%, respectively.[9] Despite the improvement in individual metrics, achieving desirable NRR activity while largely suppressing HER still remains a challenge. Glassy materials, also called amorphous materials, offer promising potential as a class of robust materials for electrochemical NRR because of their unique features, such as disordered arrangement of atoms and outstanding corrosion resistance.[10] In particular, the abundant dangling bonds of the glassy material provide more defect sites than its crystalline counterpart and serve as trap sites to capture metastable electrons and inert gas molecules, resulting in enhanced adsorption on the catalysts.[11] It is also possible to transfer electrons into the antibonding orbital of the N≡N triple bond, causing an increase in energy and hence activating the adsorbed N_2.[12] Therefore, creating materials with more active sites via amorphization can be a desirable strategy to enhance nitrogen adsorption and suppress hydrogen adsorption for boosting NRR catalysis.

Herein, a class of glassy bullet-like MTe (M=Ru, Rh, Ir) porous nanorods (PNRs) were synthesized by using a facile large-scalable hydrothermal method as superior NRR electrocatalysts. The optimized $IrTe_4$ PNRs have demonstrated excellent NRR activities with the highest FE and NH_3 yield of up to 15.3% and 51.1 μg h^{-1} $mg^{-1}_{cat.}$, respectively, which outperform many reported NRR catalysts (Table S1). The $IrTe_4$ PNRs also show long-term

stability up to 20 consecutive cycles with no obvious activity degradation. The strong adsorption between nitrogen species and catalyst is the main reason for increasing NRR activity while suppressing HER performance, as revealed by both the N_2 temperature-programmed desorption (N_2-TPD) and valence band X-ray photoelectron spectroscopy (VB XPS). Density Functional Theory (DFT) calculations further demonstrated that the glassy $IrTe_4$ PNRs have excellent NRR selectivity with the lowest energy barrier for NRR and the highest energy barrier for HER when compared with those of $RhTe_4$ PNRs and $RuTe_4$ PNRs, ultimately leading to high NRR activity and selectivity of $IrTe_4$ PNRs.

Results and Discussion

An efficient hydrothermal approach was used to prepare the glassy $IrTe_4$ PNRs by using potassium tellurite (K_2TeO_3) and sodium hexachloroiridate (III) hydrate ($Cl_6H_2IrNaO_3$) as metal precursors. Morphology and structure of $IrTe_4$ PNRs were characterized by high-angle annular dark-field scanning transmission electron microscopy (HAAD-STEM) (**Figure 1a**). It is clearly shown that the products exhibit a one-dimensional nanostructure with the average diameter and length of 16.7 ± 2.6 nm and 96.8 ± 6.5 nm, respectively. When the TEM image of $IrTe_4$ PNRs was amplified, the porous bullet-like profile was clearly observed (Figure 1b and Figure S1). As shown in Figure 1c, a large number of blurred regions without regular atomic arrangement can be observed by high-resolution TEM (HRTEM), implying that the $IrTe_4$ PNRs are glassy. Selected-area electron diffraction (SAED) pattern revealed a halo image of concentric circles, which is also a typical feature of glassy materials (inset in Figure 1c). To further investigate the crystalline structure of this unique porous structure, powder X-ray diffraction (PXRD) was performed. As shown in Figure 1d, no diffraction peaks could be found for $IrTe_4$ PNRs, which is consistent with the HRTEM image. The molar ratio of Ir/Te was 1:4, as determined by scanning electron microscopy energy-dispersive X-ray spectroscopy (SEM-EDS) and inductively coupled plasma atomic emission spectrometry

(ICP-AES) (Figure 1e and Table S2). The STEM-EDS element mappings revealed that Ir and Te were distributed evenly in the PNRs (Figure 1f). All the detailed characterizations collectively confirmed the successful creation of glassy $IrTe_4$ PNRs.

Importantly, the synthetic method is versatile and can be extended to other tellurides, such as $RuTe_4$ and $RhTe_4$. Interestingly, the $RuTe_4$ PNRs and $RhTe_4$ PNRs were successfully created with similar profiles as $IrTe_4$ PNRs (**Figure 2a,e** and Figure S2). The HRTEM images showed a large number of fuzzy areas without clear lattice fringes (Figure 2b,f). Further, the findings of the SAED images are consistent with those of glassy materials (Figure S3). To further confirm the glassy feature of $RuTe_4$ PNRs and $RhTe_4$ PNRs, PXRD characterizations were carried out; only a featureless pattern can be observed without obvious diffraction peaks (Figure 2c,g). The molar ratios of $RuTe_4$ PNRs and $RhTe_4$ PNRs were also each approximately 1:4 and only a slightly increased size can be observed for $RhTe_4$ PNRs (Figure S4, S5 and Table S2). Their element distributions were revealed by STEM-EDS element mappings, in which the Ru/Rh and Te were distributed uniformly along the PNRs (Figure 2d,h). Additionally, Te NWs and IrTe PNRs with different molar ratios were also prepared as catalytic references (Figure S6-8). Since similar Ir, Ru, and Rh NWs could not be generated without the addition of potassium tellurite (Figure S9), we prepare the Ir PNRs by electrochemical etching of $IrTe_2$ PNRs under 1.0 M KOH solution for 500 cyclic voltammograms (Figure S10).

To assess electrocatalytic activity, the NRR measurements of MTe PNRs were carried out in 0.1 M KOH with a typical H-type cell. The polarization curves of various catalysts were obtained by using the linear sweeping voltammetry method (**Figure 3a**). Compared with $IrTe_4$ PNRs and Te NWs, an obvious enhanced current density under the same conditions can be observed for $RuTe_4$ PNRs and $RhTe_4$ PNRs, suggesting that the different current response for MTe PNRs. The chronoamperometry method was used to further explore the NRR performances under different potentials (Figure S11). The products of NH_3 and hydrazine

(N_2H_4) were analyzed by spectrophotometry (Figure S12, 13). The average yields of NH_3 are shown in Figure 3b, where the $IrTe_4$ PNRs exhibited a volcano-like FE_{NH3} as a function of applied voltage. Clearly, the $IrTe_4$ PNRs showed the highest FE_{NH3} (15.3%) and the highest NH_3 yield (51.1 μg h^{-1} $mg^{-1}_{cat.}$) at -0.2 V versus a reversible hydrogen electrode (vs. RHE), which are superior to those of many reported NRR electrocatalysts (Table S1). A slow activity decline was observed when the applied voltages were increased, which is likely caused by the competitive adsorption of hydrogen and nitrogen species on the catalytic sites (Figure S14).[13] Very small amounts of N_2H_4 as byproducts were detected in the electrolyte at different potentials (Figure S15). For comparison, NRR measurements for $RuTe_4$ PNRs, $RhTe_4$ PNRs, Ir PNRs and Te NWs were also carried out in similar conditions. We can see that all MTe_4 PNRs showed greatly enhanced NRR performances compared with Te NWs (8.0 μg h^{-1} $mg^{-1}_{cat.}$). The average NH_3 yields of $RuTe_4$ PNRs and $RhTe_4$ PNRs were 30.4 μg h^{-1} $mg^{-1}_{cat.}$ and 43.7 μg h^{-1} $mg^{-1}_{cat.}$, respectively, which are lower than that of $IrTe_4$ PNRs (51.1 μg h^{-1} $mg^{-1}_{cat.}$) at -0.2 V vs. RHE. The $RuTe_4$ PNRs and $RhTe_4$ PNRs exhibited reduced FE_{NH3} due to the competitive adsorption of hydrogen species on $RuTe_4$ PNRs and $RhTe_4$ PNRs, which is higher than that of $IrTe_4$ PNRs (Figure 3c and Figure S16). Similarly, $RuTe_4$ PNRs and $RhTe_4$ PNRs also showed the highest average NH_3 yield and FE at -0.2 V vs. RHE (Figure S17a,b). To obtain the optimized IrTe PNRs for NRR, the IrTe PNRs with different molar ratio of Ir/Te were further tested (Figure S17c,d). The $IrTe_2$ PNRs exhibited unsatisfactory activity with low NH_3 yield and small FE, which were significantly inferior to those of $IrTe_4$ PNRs. For $IrTe_8$ PNRs, significant NH_3 yields and FE decreases can also be observed, demonstrating that the presence of the appropriate concentration of Ir plays a key role in N_2 fixation. Indeed, excessive Ir favors the competitive adsorption of hydrogen species, which results in a remarkable FE_{NH3} decrease but a significant FE_{H2} enhancement (Figure S18). The sharply decrease in NH_3 FE and the significantly increased H_2 yield and FE_{H2} of Ir PNRs demonstrate that pure Ir favors hydrogen production (Figure S19). The NH_3 yield and corresponding

FE_{NH3} of $IrTe_4$ PNRs at -0.2 V vs. RHE have been carried out at different N_2 flow rates. However, the similar NH_3 yield and FE demonstrate that the NRR performance is independent of the gas flow rate (Figure S20). To prove the NH_3 generated from NRR process catalyzed by $IrTe_4$ PNRs, ^1H nuclear magnetic resonance (NMR) was used to analyze the electrolyte by using $^{14}N_2$ and $^{15}N_2$ as feeding gas, respectively (Figure 3d and Figure S21). Additionally, $^{14}NH_4Cl$ and $^{15}NH_4Cl$ were performed as a reference. The signals were further split, which was caused by mutual interference of hydrogen on the ammonium ions.[14] The coupling constant of 53.0 Hz can be observed for $^{14}NH^{4+}$ when employed $^{14}N_2$ as feeding gas, which is the same as that of $^{14}NH_4^+$. However, the NMR spectra of the electrolyte after electrolysis under $^{15}N_2$ atmosphere show a similar coupling constant and peak shapes as commercial $^{15}NH_4^+$, demonstrating that the NH_3 was indeed produced during the NRR process. Finally, a control experiment was also conducted under Ar flow, where the negligible UV-vis absorbance of NH_3 and N_2H_4 confirmed that the nitrogen source was derived from the supplied N_2 (Figure S22). Additionally, no obvious $^{14}NH_4^+$ NMR signal can be detected when N_2 was electrolyzed by $IrTe_4$ PNRs at open circuit, demonstrating negligible solvent residues (Figure S23).

To explore the durability of $IrTe_4$ PNRs, cycling tests of $IrTe_4$ PNRs at -0.2 V vs. RHE were performed (Figure 3e). No significant fluctuations in NH_3 yield and corresponding FE were found after 20 consecutive cycles, which is a result of the outstanding chemical stability and strong corrosion resistance of glassy materials.[15] The high catalytic durability was also confirmed by chronoamperometry measurements, where limited current change was observed after 40 h at -0.2 V vs. RHE (Figure S24). Moreover, the yield of NH_3 increased as the electrolysis time, further demonstrating the excellent stability of $IrTe_4$ PNRs (Figure S25-S26). To determine the morphological and structural stability, detailed characterizations of $IrTe_4$ PNRs were performed. Only Te (0) XPS peaks were reduced, indicating that negligible change in the electronic structure occurred during the catalysis, but a small amount of Te (0)

was dissolved (Figure S27). In addition, the porous $IrTe_4$ PNRs with bullet-like profile and glassy feature were largely maintained. The STEM-EDS elements mappings of $IrTe_4$ PNRs revealed that the Ir and Te were still distributed homogenously along the PNRs (Figure S28).

To evaluate the intrinsic activity of MTe PNRs, the double-layer capacitance (C_{dl}) was performed in Figure S29, which is correlated with the electrochemical active surface area.[16] The C_{dl} values increased from $IrTe_4$ PNRs to $RhTe_4$ PNRs and $RuTe_4$ PNRs, indicating that ECSA improved HER process rather than NRR. The adsorption of intermediate species on the catalytic sites, as a crucial factor for electrocatalysis, is closely related to the valence electron state of catalysts. The average energy of the *d*-electron is employed as a practical means to predicate and describe the binding strength between the catalyst and the adsorbate.[17] Generally, a higher *d*-band center (relative to the Fermi level) represents a stronger adsorbing ability.[18] To this end, VB XPS measurements of various catalysts were made (**Figure 4a**). Compared with Te NWs, the *d*-band center of MTe_4 PNRs gradually shifted to the Fermi level, indicating the enhanced binding strength after incorporation of different metals, in which the $IrTe_4$ PNRs showed the strongest affinity for the adsorbed species. Moreover, considering the connection between binding strength and NRR performance, the volcano map is established as a function of the *d*-band center for comparison (Figure 4b). Specifically, $IrTe_4$ PNRs with the highest NH_3 yield exhibited the lowest *d*-band center (relative to the Fermi level), suggesting that the strong adsorbing ability is the key to promote the NRR activity. To further demonstrate the strong chemical adsorption of N_2 on MTe_4 PNRs, N_2-TPD was performed. As shown in Figure 4c, the N_2 desorption peak of Te NWs was located at 440 °C. Interestingly, the peaks appeared at higher temperature after incorporation of different metals, in which the adsorption peak of $IrTe_4$ PNRs was located at the highest temperature, indicating the strong chemical adsorption between N_2 and $IrTe_4$ PNRs. Based on the above analysis, a possible associative alternating pathway for $IrTe_4$ PNRs can be depicted by a schematic diagram (Figure 4d). Specifically, when N_2 approaches the surface of the $IrTe_4$ PNRs, nitrogen species

tend to be adsorbed on the catalytic sites on account of their *d*-band center being close to the Fermi level, endowing them with a stronger absorbability to N_2. Then, a single hydrogenation step alternately occurs on two N atoms to break the N≡N triple bond and form a N-H bond. Subsequently, two NH_3 molecules are successively released from the surface of the $IrTe_4$ PNRs in preference to N_2H_4 due to the strong chemisorption between catalyst and nitrogen species.

DFT calculations reveal the electroactivity comparison between glassy MTe porous structures. All the glassy structures show abundant varied coordinated transition metals within the highly disordered lattice, supporting the loss of crystalline. Compared to $RhTe_4$ and $RuTe_4$, the electronic distribution in $IrTe_4$ shows slightly stronger mixing of anti-binding and bonding orbitals near Fermi level (E_F), indicating efficient electron transfer between Rh and surrounding Te atoms (Figure S30). Though the overall d-band center has been characterized by the XPS, the detailed look into the individual electronic structures of metal and Te are still needed. The projected partial density of states (PDOS) shows that the Ir-5d bands show the dominant peak at the lowest position, indicating a relatively electron-rich character. On the contrary, the dominant bands of Ru-4d bands occupy the highest position near the Fermi level (E_F) (**Figure 5a**). Meanwhile, the Te-4p bands display the opposite trend with the d-band PDOS, in which the Te-4p bands in $IrTe_4$ are the most electroactive with highest position of the dominant peak. More importantly, the Te-4p bands cross the E_F, supporting the electro-activation of Te in the glassy IrTe PNR (**Figure 5b**). The PDOS of key reactants H_2O shows a good orbital overlapping with the Ir-5d bands, demonstrating a good H_2O dissociation ability for the consecutive NRR process. The N_2 bands show a similar gap with the d bands of the glassy MTe PNR (**Figure 5c**). Thus, we have supplied the proposed mechanism to illustrate the superior NRR performance of IrTe PNR. Ir plays as the electron magnet to fix H_2O and dissociate the H-O bonds for NRR process in the alkaline environment. The surrounding electroactive Te atoms significantly pump the electrons towards the adsorbates N_2 for further

efficient hydrogenation (**Figure 5d**). The optimized structural configurations of the optimal adsorption sites also support the proposed mechanism (**Figure 5e**).

Additionally, we investigate the superior NRR performance from energetic view. Notably, the initial hydrogenation of $IrTe_4$ PNR shows is more energetically favorable. The largest reaction barrier occurs at the final formation of the second NH_3 with a barrier height of 0.44 eV. On the contrary, the $RuTe_4$ PNR shows the largest energetic barrier of 0.88 eV at the formation of [$*NH_2$], which is much larger than that of IrTe4 PNR. The $RhTe_4$ PNR shows a similar performance with $RuTe_4$ PNR, which is consistent with the experiments. Therefore, the $IrTe_4$ shows the lowest overpotential, which guarantees efficient NRR (**Figure 5f**). In addition, the adsorption of both N_2 and H_2O are critical to guarantee an efficient NRR. $IrTe_4$ PNR shows the evident advantages in adsorption of N_2 and H_2O with the lowest energies, confirming their superior NRR performance (**Figure 5g**). In the end, we also consider the competitive HER process. In both $RuTe_4$ PNR and $RhTe_4$ PNR, HER is much more favorable than the NRR process with a much lower energy barrier of 0.17 eV and 0.20 eV, respectively. However, $IrTe_4$ PNR shows the much larger energy barrier of HER in alkaline media of 0.33 eV. The overall endothermic HER process in $IrTe_4$ PNR enhances the performance of NRR based on the evidential suppression of HER (**Figure 5h**). Thus, the FE_{NH3} of MTe_4 PNRs in the experimental observation followed by $IrTe_4$ PNRs > $RhTe_4$ PNRs > $RuTe_4$ PNRs is highly consistent with the electronic structure environment with the corresponding adsorption behaviors.

Conclusion

In summary, we have successfully explored and demonstrated a universal approach to create glassy bullet-like MTe PNRs (M=Ru, Rh, Ir) as efficient NRR electrocatalysts. Notably, all the glassy MTe PNRs exhibited robust performance for N_2 electroconversion, in which the

$IrTe_4$ PNRs showed superior NRR performance with the highest NH_3 FE (15.3%) and NH_3 yield (51.1 μg h^{-1} $mg^{-1}_{cat.}$) as well as low FE for HER, simultaneously realizing enhanced NH_3 conversion efficiency and suppressed HER process. Importantly, the $IrTe_4$ PNRs can also last up to 20 consecutive cycles with no significant performance degradation. We found that the enhanced NRR process and suppressed HER pathway can be attributed to the strong adsorbing ability of the nitrogen species on the catalysts. DFT calculations explain the reaction mechanism of alkaline NRR in $IrTe_4$ PNR regarding both electronic structure and energetic pathway, in which Ir dissociates the H_2O and pump the electrons to Te for stable fixation of N_2. The efficient electron transfer on the glassy $IrTe_4$ PNR leads to the remarkable performance of NRR. This work provides a new perspective to develop high-performance catalysts with glassy structure for enhanced electrocatalysis and beyond.

Acknowledgements

This work was financially supported by the Ministry of Science and Technology of China (2016YFA0204100, 2017YFA0208200), the National Natural Science Foundation of China (21571135), Young Thousand Talented Program, the Natural Science Foundation of Jiangsu Higher Education Institutions (17KJB150032), the project of scientific and technologic infrastructure of Suzhou (SZS201708), the Priority Academic Program Development of Jiangsu Higher Education Institutions (PAPD), and start-up support from Soochow University.

Conflict of Interest

The authors declare no conflict of interest.

[1] a) S. Andersen, V. Čolić, S. Yang, J. A. Schwalbe, A. C. Nielander, J. M. McEnaney, K. Enemark-Rasmussen, J. G. Baker, A. R. Singh, B. A. Rohr, M. J. Statt, S. J. Blair, S. Mezzavilla, J. Kibsgaard, P. C. K. Vesborg, M. Cargnello, S. F. Bent, T. F. Jaramillo, I.

E. L. Stephens, J. K. Nørskov, I. Chorkendorff, *Nature* DOI: 10.1038/s41586-019-1260-x 96-99; b) J. B. Spinelli, H. Yoon, A. Ringel, S. Jeanfavre, C. Clish, M. Haigis, *Science* **2017**, *358*, 941-946; c) L. Zhang, L. X. Ding, G. F. Chen, X. Yang, H. Wang, *Angew. Chem. Int. Ed*. **2019**, *58*, 2612-2616; d) Y. C. Hao, Y. Guo, L. W. Chen, M. Shu, X. Y. Wang, T. A. Bu, W. Y. Gao, N. Zhang, X. Su, X. Feng, J. W. Zhou, B. Wang, C. W. Hu, A. X. Yin, R. Si, Y. W. Zhang, C. H. Yan, *Nat. Catal.* **2019**, *2*, 467.

[2] E. E. Stüeke, R. Buick, B. M. Guy, M. C. Koehler, *Nature* **2015**, *359*, 666-669.

[3] a) J. A. Pool, E. Lobkovsky, P. J. Chirik, *Nature* **2004**, *427*, 527-530; b) J. G. Chen, R. M. Crooks, L. C. Seefeldt, K. L. Bren, R. M. Bullock, M. Y. Darensbourg, P. L. Holland, B. Hoffman, M. J. Janik, A. K. Jones, M. G. Kanatzidis, P. King, K. M. Lancaster, S. V. Lymar, P. Pfromm, W. F. Schneider, R. R. Schrock, *Science* **2018**, *360*, eaar6611.

[4] a) X. Liu, H. Jang, P. Li, J. Wang, Q. Qin, M. G. Kim, G. Li, J. Cho, *Angew. Chem. Int. Ed*. DOI: 10.1002/anie.201906521; b) Z. Geng, X. Kong, P. Li, K. Li, Z. Liu, Z. Du, M. Shu, R. Si, J. Zeng, *Adv. Mater.* **2018**, *30*, 1803498; c) B. R. Suryanto, H. L. Du, D. Wang, J. Chen, A. Simonov, D. MacFarlane, *Nat. Catal.* **2019**, *2*, 290-296.

[5] J. Zhao, A. S. Goldman, J. F. Hartwig, *Science* **2005**, *307*, 1080-1082.

[6] Y. Yao, S. Zhu, H. Wang, H. Li, M. Shao, *J. Am. Chem. Soc.* **2018**, *140*, 1496-1501.

[7] a) H. P. Jia, E. A. Quadrelli, *Chem. Soc. Rev.* **2014**, *43*, 547-564; b) K. Honkala, A. Hellman, I. N. Remediakis, A. Logadottir, A. Carls-son, S. Dahl, C. H. Christensen, J. K. Nørskov, *Science* **2005**, *307*, 555-558; c) J. S. Anderson, J. Rittle, *Nature* **2013**, *501*, 84-87.

[8] C. Guo, J. Ran, A. Vasileff, S. Z. Qiao, *Energy Environ. Sci.* **2018**, *11*, 45-56.

[9] H. Jin, L. Li, X. Liu, C. Tang, W. Xu, S. Chen, L. Song, Y. Zheng, S. Z. Qiao, *Adv. Mater.* **2019**, 1902709.

[10] a) J. M. V. Nsanzimana, Y. Peng, Y. Y. Xu, L. Thia, C. Wang, B. Y. Xia, X. Wang, *Adv. Energy Mater.* **2018**, *8*, 1701475; b) M. Z. Rahman, P. C. Tapping, T. W. Kee, R.

Smernik, N. Spooner, J. Moffatt, Y. Tang, K. Davey, S. Z. Qiao, *Adv. Funct. Mater.* **2017**, *27*, 1702384; c) N. Yang, H. Cheng, X. Liu, Q. Yun, Y. Chen, B. Li, B. Chen, Z. Zhang, X. Chen, Q. Lu, J. Huang, Y. Huang, Y. Zong, Y. Yang, L. Gu, H. Zhang, *Adv. Mater.* **2018**, *30*, 1803234; d) Y. Lu, J. Wang, Y. Peng, A. Fisher, X. Wang, *Adv. Energy Mater.* **2017**, *7*, 1700919; e) X. Zhang, Z. Luo, P. Yu, Y. Cai, Y. Du, D. Wu, S. Gao, C. Tan, Z. Li, M. Ren, T. Osipowicz, S. Chen, Z. Jiang, J. Li, Y. Huang, J. Yang, Y. Chen, C. Y. Ang, Y. Zhao, P. Wang, L. Song, X. Wu, Z. Liu, A. Borgna, H. Zhang, *Nat. Cat.* **2018**, *1*, 452-459.

[11] a) J. Zhang, Y. Hu, D. Liu, Y. Yu, B. Zhang, *Adv. Sci.* **2017**, *4*, 1600343; b) C. Lv, C. Yan, G. Chen, Y. Ding, J. Sun, Y. Zhou, G. Yu, *Adv. Mater.* **2018**, *130*, 1-5; c) Y. Zhou, S. Sun, J. Song, S. Xi, B. Chen, Y. Du, A. C. Fisher, F. Cheng, X. Wang, H. Zhang, Z. J. Xu, *Adv. Mater.* **2018**, *30*, 1802912; d) R. Wu, J. Zhang, Y. Shi, D. Liu, B. Zhang, *J. Am. Chem. Soc.* **2015**, *137*, 6983-6986; e) T. Zhang, M. Y. Wu, D. Y. Yan, J. Mao, H. Liu, W. B. Hu, X. W. Du, T. Ling, S. Z. Qiao, *Nano Energy* **2018**, *43*, 103-109.

[12] N. Zhang, A. Jalil, D. Wu, S. Chen, Y. Liu, C. Gao, W. Ye, Z. Qi, H. Ju, C. Wang, X. Wu, L. Song, J. Zhu, Y. J. Xiong, *J. Am. Chem. Soc.* **2018**, *140*, 9434-9443.

[13] T. Oshikiri, K. Ueno, H. Misawa, *Angew. Chem. Int. Ed*. **2016**, *55*, 3942-3946.

[14] a) Q. Qin, Y. Zhao, M. Schmallegger, T. Heil, J. Schmidt, R. Walczak, G. Gescheidt-Demner, H. Jiao, M. Oschatz, *Angew. Chem. Int. Ed*. **2019**, *58*, 2-8; b) N. Cao, Z. Chen, K. Zang, J. Xu, J. Zhong, J. Luo, X. Xu, G. Zheng, *Nat. Commun*. **2019**, *10*, 2877.

[15] S. Yan, K. P. Abhilash, L. Tang, M. Yang, Q. Xia, Q. Guo, H. Xia, *Small* **2018**, *15*, 1804371.

[16] A. Zhang, R. He, H. Li, Y. Chen, T. Kong, K. Li, H. Ju, J. Zhu, W. Zhu, J. Zeng, *Angew. Chem. Int. Ed*. **2018**, *57*, 10954-10958.

[17] J. K. Nørskov, *Adv. Catal.* **2000**, *45*, 71-129.

[18] J. K. Nørskov, *Nat. Chem.* **2009**, *1*, 37-46.

FIGURES

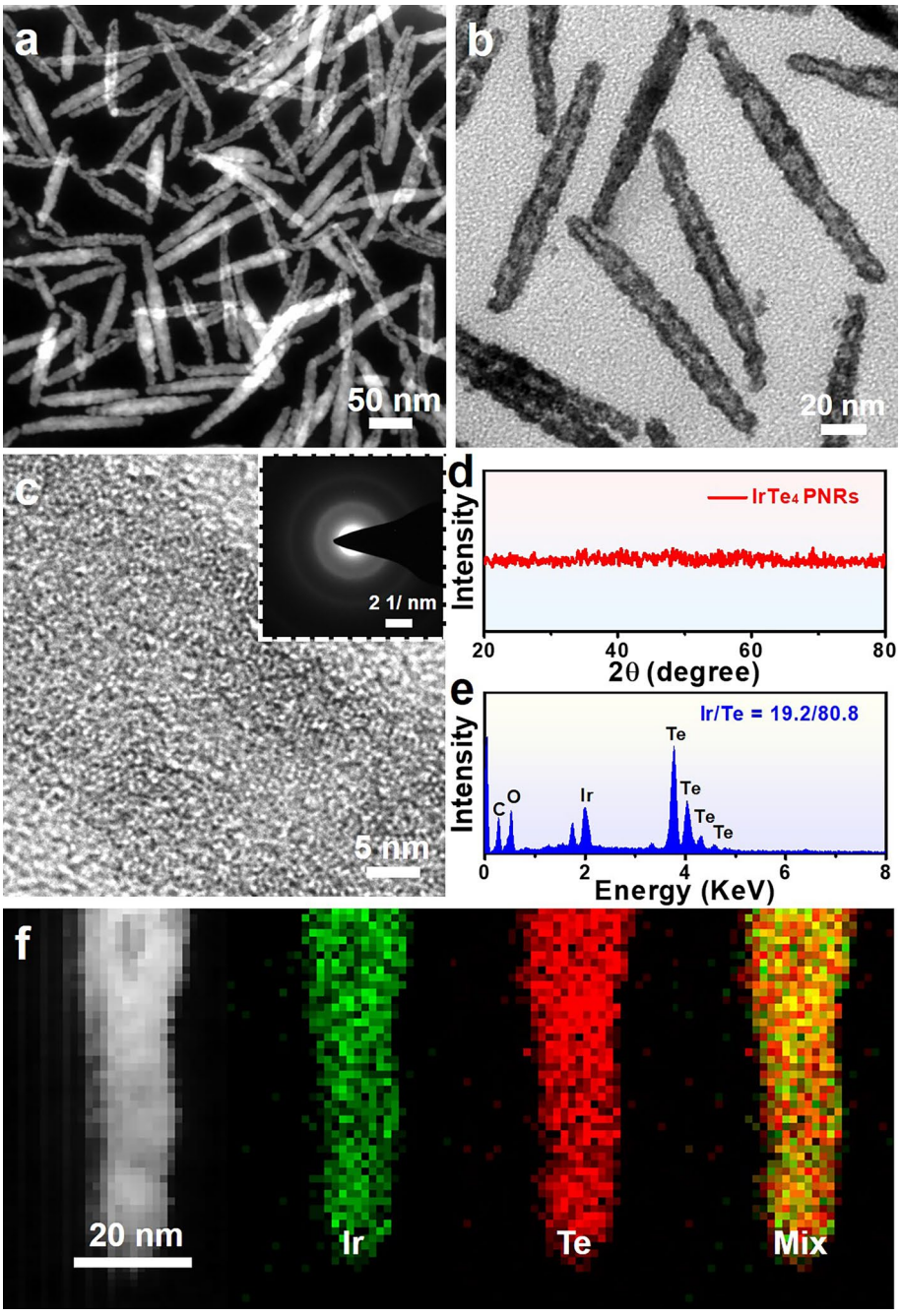

Figure 1. (a) HAAD-STEM image, (b) TEM image, (c) HRTEM image, (d) PXRD pattern, (e) SEM-EDS spectrum and (f) STEM-EDS element mappings of $IrTe_4$ PNRs. The inset in (c) is the SAED pattern of $IrTe_4$ PNRs.

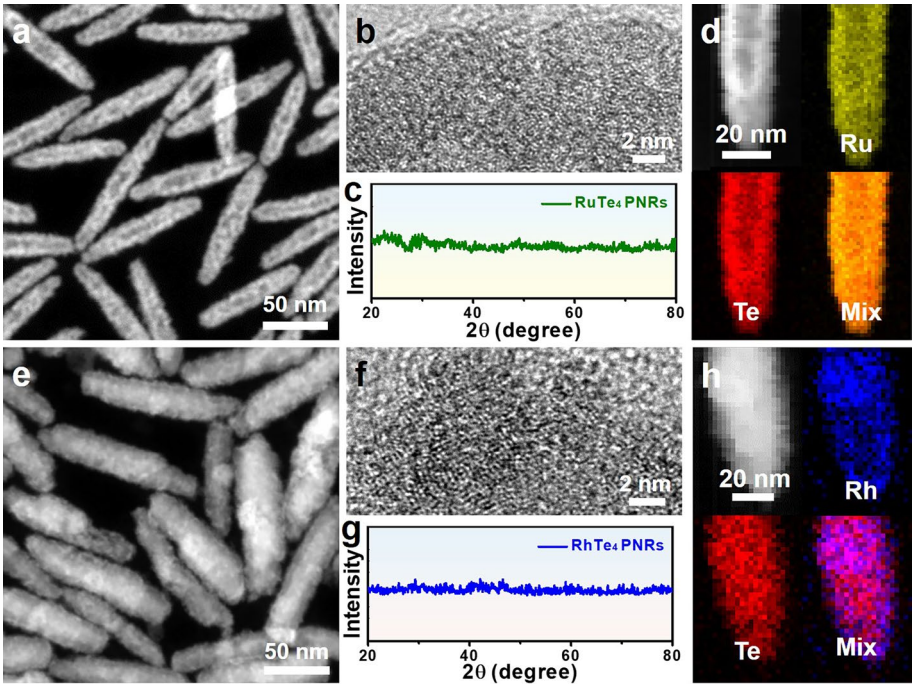

Figure 2. (a) HAAD-STEM image, (b) HRTEM image, (c) PXRD pattern and (d) STEM-EDS element mappings of $RuTe_4$ PNRs. (e) HAAD-STEM image, (f) HRTEM image, (g) PXRD pattern and (h) STEM-EDS element mappings of $RhTe_4$ PNRs.

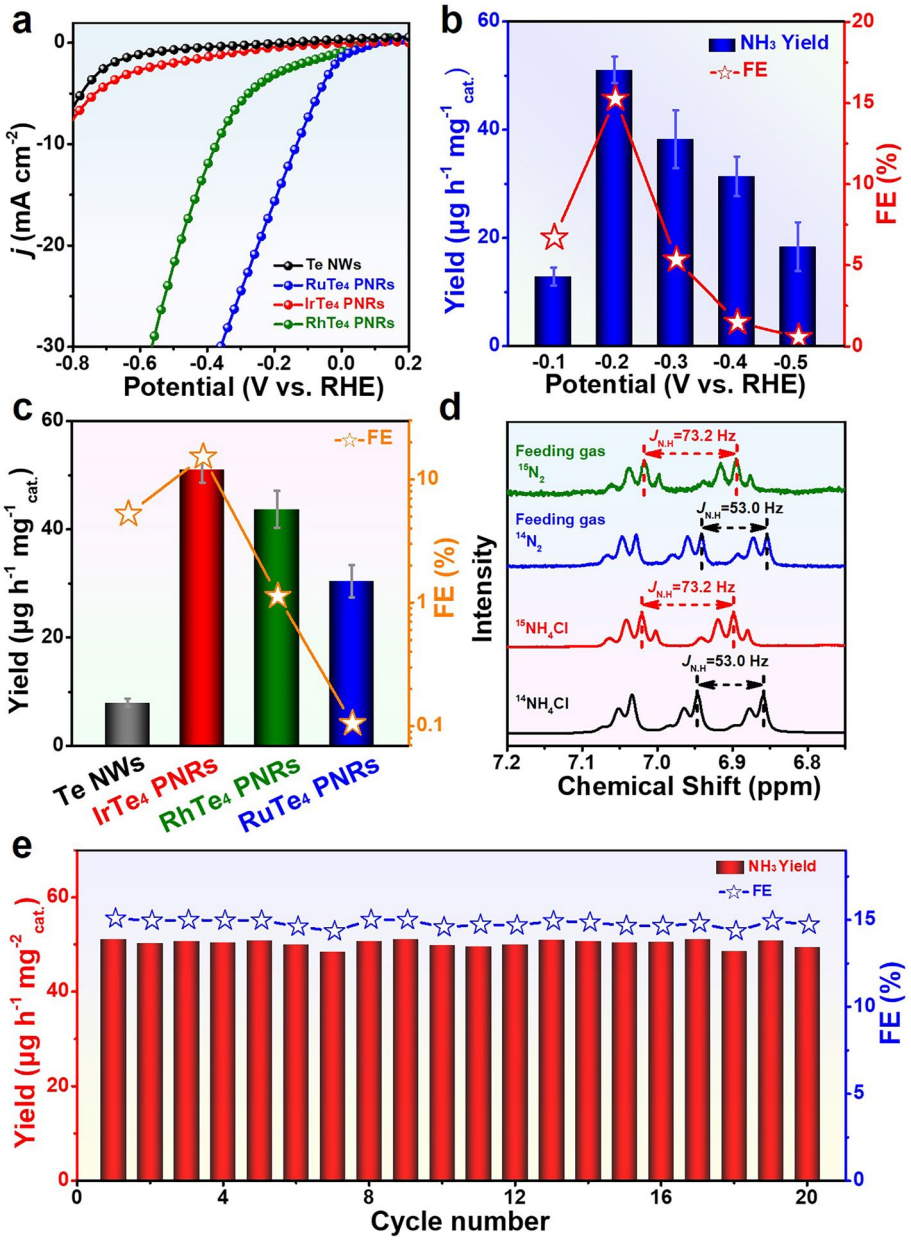

Figure 3. (a) Polarization curves of MTe_4 PNRs under ambient conditions. (b) Histograms of average NH_3 yield rate and corresponding FE at different applied potentials. (c) His-tograms of average NH_3 yield rate and corresponding FE of various catalysts at -0.2 V vs. RHE. (d) ^1H NMR spectra of $^{14}NH_4Cl$ and $^{15}NH_4Cl$, and the electrolyte produced from the NRR test of $IrTe_4$ PNRs by using $^{14}N_2$ and $^{15}N_2$ as feeding gas. (e) Cycling test of $IrTe_4$ PNRs at -0.2 V vs. RHE.

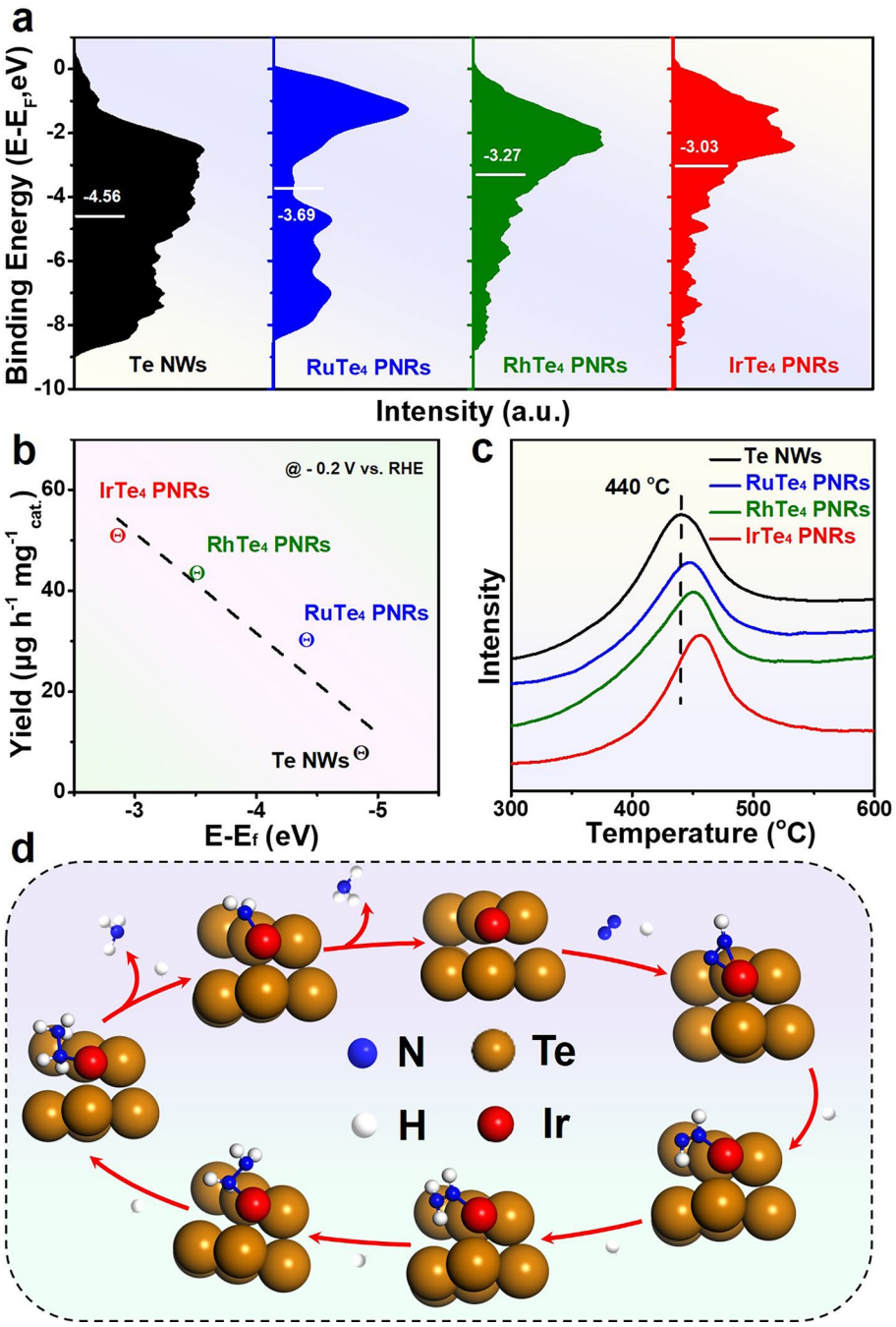

Figure 4. (a) Surface valence band photoemission spectra of MTe_4 PNRs. The white bars in (a) highlight the *d*-band center of MTe_4 PNRs. (b) NH_3 yield of MTe_4 PNRs (at -0.2 V vs. RHE) as a function of the $E\text{-}E_f$ parameter. (c) The N_2-TPD profiles of MTe_4 PNRs. (d) Schematic depiction of the proposed mechanism for NRR on $IrTe_4$ PNRs. The blue, orange, white, and red balls represent the N, Te, H and Ir atoms, respectively.

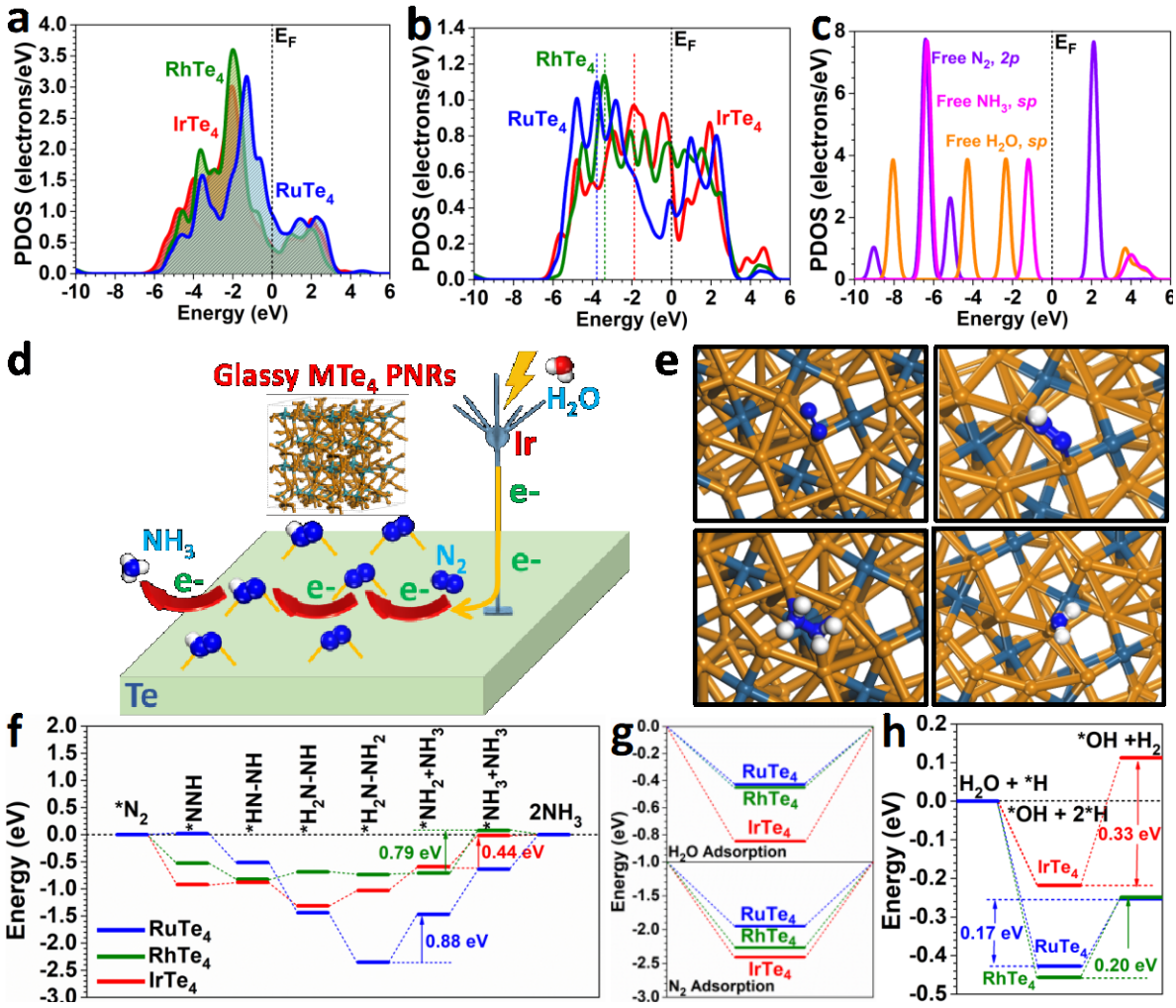

Figure 5. (a) The PDOS of d band. (b) The PDOS of 4p band of Te. (c) The PDOS of key adsorbates in NRR. (d) The proposed electron transfer mechanism in the MTe PNR. (e) Optimized configuration of key adsorbates. (f) Energetic diagram of NRR of MTe PNRs. (g) Adsorption energy comparisons of N_2 and H_2O. (h) The energetic pathway of HER in the MTe PNR.

A General Strategy to Glassy M-Te (M=Ru, Rh, Ir) Porous Nanorods as Efficient Electrocatalysts for N_2 Reduction

*Juan Wang, Yujin Ji, Rongguan Yin, Xing Zhu, Youyong Li, Qi Shao, and Xiaoqing Huang**

TOC figure

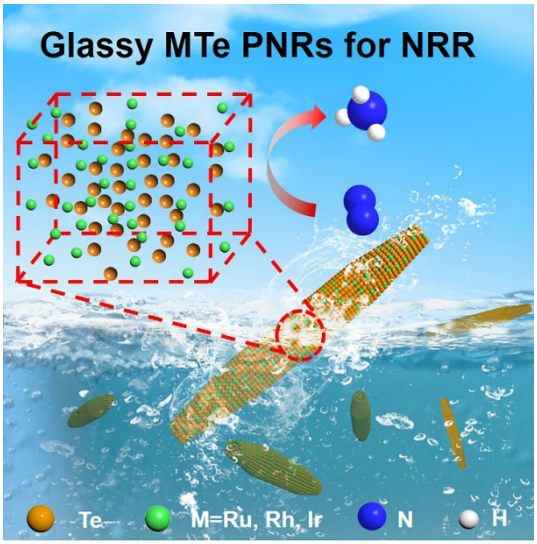

Glassy MTe porous nanorods (PNRs) with bullet-like profile were successfully synthesized for the first time, and adopted as as efficient electrocatalysts for N_2 reduction reaction (NRR). Due to their energetic-favorable NRR pathway and suppressed HER process, the optimized $IrTe_4$ PNRs present superior activity with the highest NH_3 yield (51.1 μg h^{-1} $mg^{-1}_{cat.}$) and Faraday efficiency (15.3%) as well as long-term stability of up to 20 consecutive cycles under ambient conditions, making them among the most active NRR electrocatalysts reported to date.